Spectrally Efficient Long-Haul Optical Networking Using 112-Gb/s Polarization-Multiplexed 16-QAM

P. J. Winzer, A. H. Gnauck, C. R. Doerr, M. Magarini, and L. L. Buhl

***Abstract*—We discuss the generation, wavelength-division-multiplexed (WDM) long-haul transmission, and coherent detection of 112-Gb/s polarization-division-multiplexed (PDM) 16-ary quadrature amplitude modulation (16-QAM) at a line rate of 14 Gbaud and spectral efficiencies beyond 4 b/s/Hz. We describe the (off-line) digital signal processing and blind filter adaptation algorithms used in our intradyne receiver and characterize its performance using both simulated and measured 16-QAM waveforms. We measure a required optical signal-to-noise ratio of 20.2 dB (0.1-nm reference bandwidth; 10^{-3} bit-error ratio), 3.2-dB off the theoretical limit. We study the effects of finite analog-to-digital converter resolution, laser frequency offset, laser phase noise, and narrowband optical filtering. Our experiments on a 25-GHz WDM grid (4.1-b/s/Hz spectral efficiency) reveal a 1-dB penalty after 7 passes though reconfigurable optical add/drop multiplexers (ROADMs) and an achievable transmission reach of 1022 km of uncompensated standard single-mode fiber. At a spectral efficiency of 6.2 b/s/Hz (16.67-GHz WDM channel spacing) a transmission reach of 630 km is attained.**

***Index Terms*—100G Ethernet, coherent detection, optical networking, optical transmission, quadrature amplitude modulation (QAM), wavelength-division multiplexing (WDM).**

I. Introduction

ENABLED by wavelength-division multiplexing (WDM), fiber-optic transport capacities have been growing exponentially over the last 20 years, just enough to meet the annual growth in data traffic of several tens of percent per year generated by our multi-media communication and information society [1]. At a fixed optical amplification bandwidth, increasing the transmission capacity requires increasing the spectral efficiency (SE), i.e., the net per-channel bit rate R_B divided by the WDM channel spacing Δf

$$\mathrm{SE} = \frac{R_B}{\Delta f}. \tag{1}$$

Up until a few years ago, virtually all optical transmission systems employed binary intensity or phase modulation [2], and the required increase in SE was satisfied by advances in high-speed electronics (higher R_B) as well as in laser- and optical-filter frequency stability (reduced Δf). In the early 2000s, the speed of opto-electronic modulation and detection approached the bandwidths of stable optical filters, and higher-order modulation formats had to be used to increase R_B at fixed signal bandwidth. This process started with differential quadrature phase shift keying (DQPSK) [3], which allowed point-to-point SEs of up to 1.6 b/s/Hz [4], and comfortably enabled optically-routed networking at 40 Gb/s on a 50-GHz WDM grid (SE of 0.8 b/s/Hz), including multiple passages though reconfigurable optical add/drop multiplexers (ROADMs) [5]. In a next step, polarization division multiplexing (PDM) was added to boost the SE to 3.2 b/s/Hz in point-to-point applications using direct detection [4], and to 2 b/s/Hz in an optically-routed environment using coherent detection [6]. Today, PDM-QPSK is considered an attractive option for 100-Gb/s optically routed transport systems.

Further compression of the signal spectrum requires higher-level (M-ary) modulation formats, beneficially in combination with coherent detection, with an SE limited to $2\log_2 M$ using PDM. In practice, and assuming optically-routed networking with multiple state-of-the-art ROADMs, ~50% of this value, i.e., $\log_2 M$ may be obtained. Furthermore, higher SEs come at the expense of increasingly more stringent signal-to-noise-ratio (SNR) requirements. This is visualized in Fig. 1 [7], where recent experimental results for quadrature amplitude modulation (QAM) are contrasted with theoretical limits for the linear communication channel. The net impact of higher SNR requirements on the achievable transmission reach depends on fiber type, amplification scheme, and impact of fiber nonlinearities [8], [9]. At 1 Gbaud, constellations as high as 128-QAM with a spectral efficiency of 9.3 b/s/Hz (including the required overhead for forward error correction, FEC) have been demonstrated [10]. At 56 Gb/s, a spectral efficiency of 7.0 b/s/Hz was obtained using PDM 32-QAM and orthogonal frequency-division multiplexing (OFDM) [11]. Note in this context that multi-tone modulation (OFDM or coherent WDM) has the same SE and SNR limits as single-carrier modulation. At 114 Gb/s, 8-PSK [12] and 8-QAM [13] have achieved SEs of 4.2 b/s/Hz for point-to-point applications (no ROADMs).

In this paper, we report on a series of experiments conducted at 112 Gb/s using PDM 16-QAM at 14 Gbaud, expanding upon our initial reports in [14]–[16]. We demonstrate long-haul optically-routed networking on a 25-GHz WDM grid, and point-to-point transmission on a 16.6-GHz grid, yielding a SE of 6.2 b/s/Hz, the highest reported for single-carrier 112-Gb/s signals.

II. 16-QAM Transmitter

The setup of our 16-QAM transmitter is shown in Fig. 2. First, four copies of a true 14-Gb/s binary pseudo-random bit sequence (PRBS) of length $2^{15}-1$ are generated and amplified using high-speed electrical driver amplifiers. Although these

Manuscript received June 26, 2009. First published September 09, 2009; current version published February 01, 2010.

P. J. Winzer, A. H. Gnauck, C. R. Doerr, and L. L. Buhl are with Bell Laboratories, Alcatel-Lucent, Holmdel, NJ 07733 USA (e-mail: peter.winzer@ieee.org).

M. Magarini is with the Politecnico di Milano, 20133 Milan, Italy.

Digital Object Identifier 10.1109/JLT.2009.2031922

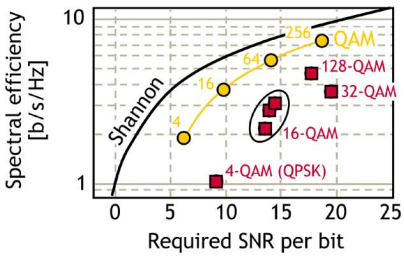

Fig. 1. Spectral efficiencies achievable as a function of required SNR per bit, referenced to a single polarization. The Shannon limit applies to ideal coding and modulation. The symbols assume QAM and enhanced FEC with 7% overhead and a 2×10^{-3} correction threshold. Circles are theoretical limits, squares represent measured points at multi-Gb/s line rates.

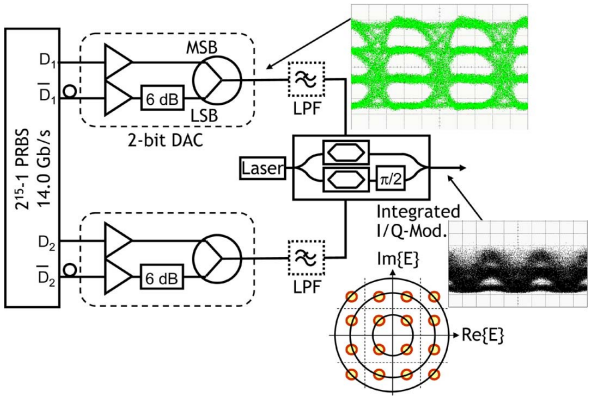

Fig. 2. Setup of the 16-QAM transmitter.

signals are still binary, signal degradations such as a reduced rise times or overshoots have to be avoided in order to keep impairments of the generated four-level signal to a minimum. For each quadrature, one binary drive bit stream is interpreted as the most significant bit (MSB), and one is attenuated by 6 dB and interpreted as the least significant bit (LSB) of a 2-bit digital-to-analog converter (DAC). MSB and LSB streams are then resistively combined with a multiple-bit decorrelation delay (12 and 18 bits, respectively) as shown in Fig. 2. An eye diagram of the four-level signals making up in-phase (I) and quadrature (Q) components of the 16-QAM signal is also shown in the figure. The peak-to-peak voltage of the four-level signals is approximately 3.5 V. In some of our experiments, the drive signals are low-pass filtered (LPF) to electrically suppress modulation sidelobes before being applied to an integrated $LiNbO_3$ double-nested Mach–Zehnder (I/Q) modulator. The 16-QAM optical intensity eye diagram with its three intensity levels corresponding to the three rings that make up a square 16-QAM constellation is also shown in Fig. 2.

As a light source, we typically use a C-band tunable external cavity laser (ECL) with a measured linewidth of ~100 kHz for the channel under test. Interfering channels use distributed feedback (DFB) lasers with linewidths of ~2 MHz. We employ two different 16-QAM transmitters of the same structure, one for the set of 'even' and one for the set of 'odd' WDM channels. Both sets are individually modulated before being combined and polarization-multiplexed, as detailed in Section V.

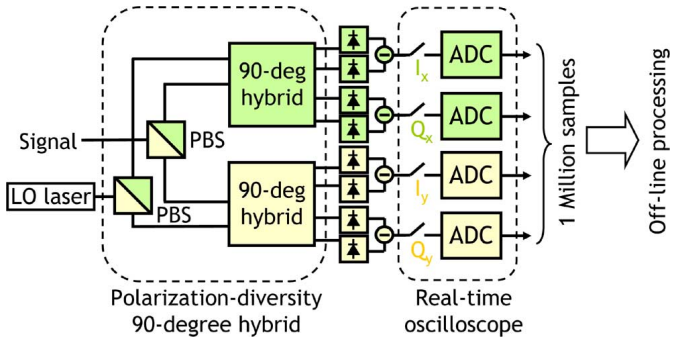

Fig. 3. Setup of the polarization-diversity coherent receiver.

III. Coherent Receiver Hardware and Algorithms

A. Opto-Electronic Receiver Front-End

The opto-electronic front-end of our intradyne receiver is shown in Fig. 3. The signal is combined with a local oscillator (LO) laser, typically the same type of ECL as used for the signal under test, in a polarization-diversity 90-degree optical hybrid. The LO is tuned to within approximately ± 20 MHz of the received signal's center frequency. The four pairs of balanced outputs from the hybrid are sampled and asynchronously digitized at 50 GSamples/s using a commercial 4-channel real-time oscilloscope, with a nominal 8-bit resolution of the analog-to-digital converters (ADCs) and a frequency-dependent effective number of bits (ENoB) between 4 and 5. All results shown here are based on offline processing of at least one million signal samples on each of the four sample streams, corresponding to more than ~250 000 received symbols (~2 million bits) for bit-error counting after the convergence of all receiver loops.

B. Receiver Digital Signal Processing

As shown in Fig. 4, the four sample streams from the ADCs are interpreted as real and imaginary parts (I and Q) of two complex sample streams, one for each polarization. In a first step, the algorithm performs ac coupling and corrects for specific (static) optical front-end errors, such as a sampling skew between I and Q signal components or phase errors within the 90-degree hybrid. Then, digital antialiasing filtering is performed. The exact antialiasing filter shape has little impact on the performance of the receiver; rectangular and Gaussian filter shapes were used. Then, a bulk chromatic dispersion (CD) filter compensates for dispersion of the transmission line. This linear filter is implemented in the frequency domain using fast Fourier transforms (FFT) and multiplication with the quadratic spectral phase characteristic of CD. Subsequently, the clock frequency is recovered by taking the FFT of the signal power waveform and detecting the pronounced 14-GHz tone. Using the recovered clock frequency, the signal is down-sampled to a synchronous 28 GSamples/s (2x oversampling at $1/\mathrm{T} = 14$ Gbaud), albeit with a yet unknown clock phase. Then, the detection algorithm performs the following tasks:

- *Source separation* to adaptively restore the original x and y polarizations of the transmit signal from the randomly rotated receive signal polarizations.

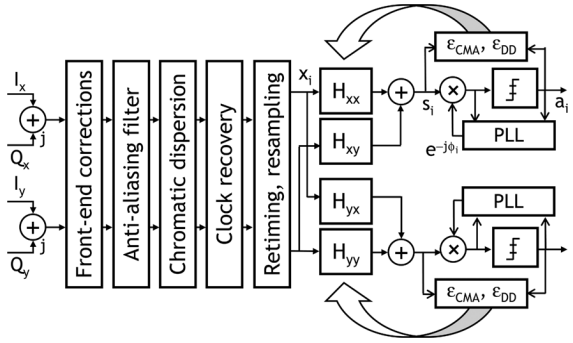

Fig. 4. Block diagram of the digital signal processing used within the coherent receiver.

- *Adaptive equalization* to counter randomly varying channel impairments.
- Recovery of the correct *sampling phase*.
- *Frequency recovery* to compensate for the residual rotation of the equalized constellation diagram due to the non-zero intermediate frequency (IF), i.e., the beat frequency between signal and LO laser.
- *Phase recovery* to keep the square QAM constellation aligned with the fixed rectangular decision boundaries (rectilinear grid in the inset to Fig. 2), which are optimum for QAM detection in the presence of circularly symmetric noise. Note that in the context of synchronization techniques for digital receivers, frequency and phase estimation are often treated together under the name of *carrier phase recovery*.

The following subsections describe these functional blocks in detail.

C. Adaptive Source Separation and Equalization

Adaptive source separation, equalization, and sampling phase recovery are simultaneously performed by the lattice filter with transfer functions $\mathrm{H_{xx}}(f), \mathrm{H_{xy}}(f), \mathrm{H_{yx}}(f)$, and $\mathrm{H_{yy}}(f)$ shown in Fig. 4, which represents the frequency-dependent inverse Jones matrix of the transmission channel. Each filter block is implemented in the time domain as a finite impulse response (FIR) filter with $\mathrm{N} = 16$ fractionally-spaced (T/2) taps, sufficient to allow for reliable operation under a pulse broadening of up to ~3 symbols [17].

In the context of this paper, we are interested in *blind* filter adaptation, i.e., adaptation without the use of a training sequence. In a first step, we use the well-proven constant modulus algorithm (CMA), a blind filter adaptation algorithm that is simple, robust, and works independent of carrier frequency and phase, both of which are initially not available to the receiver [17]–[19]. In essence, the CMA minimizes the time-averaged error

$$\langle \varepsilon_{\mathrm{CMA}} \rangle = \langle R^2 - |s_i|^2 \rangle, \tag{2}$$

reflecting the average distance of the equalized received symbols s_i (i being the symbol time index) at the output of the filter from a single circle of radius R in the complex plane ('*constant modulus*'). The filter coefficients are adapted according to

$$h^k \mapsto h^k + \mu \varepsilon_{\mathrm{CMA}} x^*_{i-k} s_i, \tag{3}$$

which minimizes $\varepsilon_{\mathrm{CMA}}$. Here, h^k stands for either $h^k_{xx}, h^k_{xy}, h^k_{yx}$ or h^k_{yy} and denotes the kth filter tap of any one of the four FIR filters; x_{i-k} denotes the (complex conjugate) signal at the equalizer input at time step i–k, and μ is a convergence parameter, typically chosen on the order of 10^{-2} for our receiver. CMA adaptation works particularly well for (single-ring) PSK constellations, where it is often the only adaptation algorithm used [20]. For QAM constellations, which are generally composed of multiple rings (cf. inset to Fig. 2), the error in Eq. (2) will not be reduced to zero by the CMA; nevertheless, minimizing the error adjusts the filter taps such that the equalized constellation becomes reasonably compact, which yields sufficient pre-convergence based on which one can safely switch to decision-directed (DD) equalization (see [17]–[19] for a discussion in single-source (non-PDM) situations). Several modifications to the CMA have also been proposed [21], [22], including radius-directed ('multi-modulus', MMA) decision-aided algorithms [23]–[26], where one first makes a decision on the ring a received symbol most likely belongs to and then adapts the equalizer using a CMA based on knowledge of the correct ring radius r_i, i.e., one uses the error $\varepsilon_{\mathrm{MMA}} = r_i^2 - |s_i|^2$. One drawback of this approach is the fact that it relies on the correct decisions regarding the transmitted ring radius; since the ring spacing in QAM is generally smaller than the minimum symbol spacing d (0.87 d and 0.54 d for square 16-QAM), these decisions show a significant number of errors for heavy noise loading and/or for severe signal distortions; in agreement with [27], we observed a reduced robustness in filter pre-convergence using the multi-ring CMA and therefore opted for the classic CMA. As a default starting condition for our regular CMA, we use unit impulses for $\mathrm{h_{xx}}$ and $\mathrm{h_{yy}}$ ($h^k_{xx} = h^k_{yy} = 1/\sqrt{2}$ for $k = \{N/2, N/2+1\}$ and zero otherwise) and all zeros for $\mathrm{h_{xy}}$ and $\mathrm{h_{yx}}$, and only change this starting condition if pre-convergence is not obtained.

After CMA pre-convergence, an initial estimate of carrier frequency offset and symbol phase was obtained as detailed in Section III.D, and filter adaptation was switched to decision-directed (DD) operation. However, instead of using standard least-mean squares (LMS) adaptation with an error signal $\varepsilon_{\mathrm{DD,standard}} = |a_i - \mathrm{e}^{-\mathrm{j}\phi} s_i|^2$, where ϕ is the correct angular back-rotation following frequency and phase tracking, we used the phase-independent error signal [28]

$$\varepsilon_{\mathrm{DD}} = |a_i|^2 - |s_i|^2 \tag{5}$$

together with the corresponding filter update algorithm

$$h^k \mapsto h^k + \mu \varepsilon_{\mathrm{DD}} x^*_{i-k} s_i, \tag{6}$$

where μ is typically chosen on the order of 10^{-4}. This filter adaptation is interleaved with a decision-directed phase-locked loop (PLL), as shown in Fig. 4. Note that the decisions a_i are

based on the (optimum) *standard rectilinear grid* of QAM decision boundaries as opposed to radial decision boundaries [23], [24]; only the *error signal* is exclusively based on radial information, which decouples the equalizer update from residual phase tracking errors within the PLL.

Throughout our experiments, we employed Gray-coded 16-QAM without differential pre-coding. Within the parameter space studied in this paper, we did not encounter any cycle slips that could lead to long error bursts when differential pre-coding is not used [29], [30]. Before outputting valid data, the receiver has to test against a short known reference pattern to determine the correct rotation of the QAM constellation. This referencing process at the receiver is regularly done in systems employing advanced modulation formats, even for simple direct-detection systems using differential phase shift keying (DPSK), where the receiver has to check for a possible pattern inversion.

D. Frequency and Phase Estimation

After CMA pre-convergence the received signal is reasonably well decomposed into its two polarizations and is roughly equalized within each polarization, but the constellation is still spinning at the IF, is wiggling due to laser phase noise, and is rotated to a random phase angle compared to the rectilinear desired decision boundaries that are aligned with the real and imaginary axes. In order to achieve frequency lock and phase alignment, a standard decision-directed PLL [19] is implemented on a block of ∼1000 symbols, as shown in Fig. 5(a). In contrast to commonly employed loop filters, our loop filter is implemented as a running average over, respectively, N_p and N_f samples of the phase difference $\Delta\phi_i$ between the pre-decision and post-decision signal samples, and the weighted output (weighting factor $0 < \alpha < 1$) of the two integrators is used as the input to the digital voltage-controlled oscillator (VCO). The parameter α is typically chosen around 0.95. The integration time constants are chosen on the order of N_p∼10 for phase estimation and N_f∼1000 for frequency estimation. In order to find the correct phase angle, we step through 10 reference constellations, rotated in increments of $\pi/20$, and pick the rotation angle of the reference constellation that shows the smallest mean-square error (cf. Fig. 5(b)). This process corresponds to a maximum likelihood (ML) search for the correct phase angle while simultaneously estimating the IF. We found this decision-directed approach to work much more reliably than multi-modulus variations of the Viterbi-Viterbi algorithm [19], [26], for the same reasons as discussed in Section III.C along with the CMA and DD filter adaptation algorithms. After initial frequency and phase lock, the decision-directed PLL continues its operation, interleaved with DD filter adaptation.

IV. Back-to-Back Characterization

A. Required Optical Signal-to-Noise Ratio (OSNR)

Fig. 6 shows back-to-back single-channel bit-error-ratio (BER) measurements of the 16-QAM signal of our initial setup [14], without electrical pre-filtering of the modulator drive signals. The single-polarization signal requires an optical

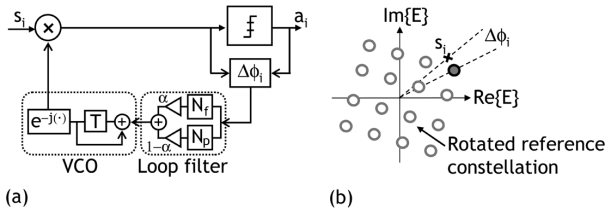

Fig. 5. (a) Decision-directed PLL; (b) In acquisition mode, a maximum-likelihood estimate is made with respect to the unknown rotation of the received constellation.

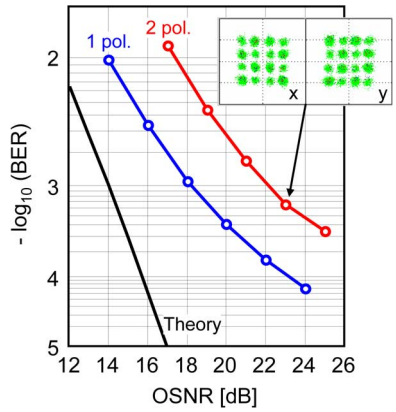

Fig. 6. Back-to-back BER measurements of our initial setup.

signal-to-noise ratio (OSNR, noise referenced to a 0.1-nm resolution bandwidth and both polarizations) of 18 dB to achieve a BER of 10^{-3}, which corresponds to an implementation penalty of about 4 dB compared to the theoretical limit [31].

Polarization multiplexing requires an OSNR of 22 dB for the measured QAM waveforms, revealing an excess penalty of 1 dB for PDM. The recovered 16-QAM signal constellations for both polarizations at 23-dB OSNR are shown as an inset to Fig. 6. Subsequent improvements to both transmitter and receiver were able to reduce the PDM excess penalty to less than 0.2 dB.

B. Parameter Sensitivities

In order to understand the sensitivity of our algorithms to various system parameters, we performed extensive Monte Carlo simulations of single-polarization coherent receiver performance. The 16-QAM waveform used for these simulations is based on 64 repetitions of a random 16-QAM sequence of length 2048, oversampled by a factor of 8. The employed modulator structure, including band-limited drive waveforms, is replicated by the simulations. The intensity eye diagram of the simulated waveform as well as the symbol constellation (including the symbol transition paths in the complex optical field plane) is shown in the inset to Fig. 7(a). We use the same algorithms for simulation as used in our experiments, and arrive at a simulated required OSNR of 14 dB at $\mathrm{BER} = 10^{-3}$, which corresponds to the theoretical limit and hence proves the absence of purely algorithm-induced sensitivity penalties in our setup.

Receiver performance as a function of the ADC resolution is shown in Fig. 7(a). Between 4 and 5 bits are needed to avoid

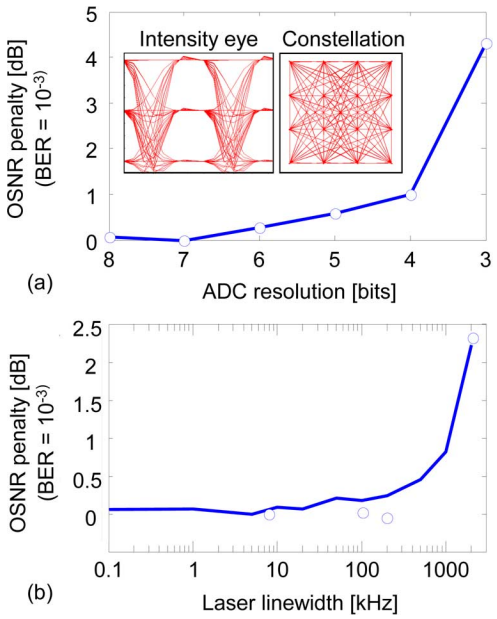

Fig. 7. (a) Simulated OSNR penalty as a function of the ADC resolution; inset: intensity eye diagram and symbol constellation with symbol transitions of simulated 16-QAM waveform; (b) Curve: Simulated OSNR penalty as a function of the aggregate laser linewidth (signal plus LO); symbols: measured OSNR penalty using lasers with different levels of phase noise.

penalties in excess of 1 dB. These values are slightly more favorable than those reported in [29]. Recall that the effective resolution provided by the real-time oscilloscope is between 4 and 5 bits.

Regarding the lock-in range of our frequency recovery loop, our simulations show negligible receiver performance degradations for values of the IF up to ∼100 MHz, also for substantial optical noise loading and typical laser linewidths of ∼100 kHz. In our experiments, we kept the IF below ∼20 MHz, which always yielded reliable frequency locking, even in the presence of severe noise loading and signal distortions.

System performance as a function of the overall laser linewidth (signal plus LO) is quantified in Fig. 7(b). The curve shows some statistical uncertainty due to the underlying Monte Carlo simulations. The sensitivity to laser phase noise closely matches the results of [30] but shows better performance than reported in [32] and [33]. The symbols in Fig. 7(b) represent measurements with different combinations of lasers, having linewidths of approximately 4 kHz, 100 kHz, and 2 MHz. In the context of our discussion on laser phase noise tolerance, we also acknowledge the fact that high-speed implementations of decision directed PLLs may require substantial parallelization and pipelining which reduces the linewidth tolerance of the system, as noted in [29]; in this case, feed-forward carrier recovery schemes can be used as a promising alternative [29], [30]. One such technique is similar to the ML technique described along with Fig. 5(b).

C. Narrow-Band Optical Filtering

Figure 8 characterizes the filtering tolerance of our setup. The shaded areas apply to simulations using super-Gaussian filters

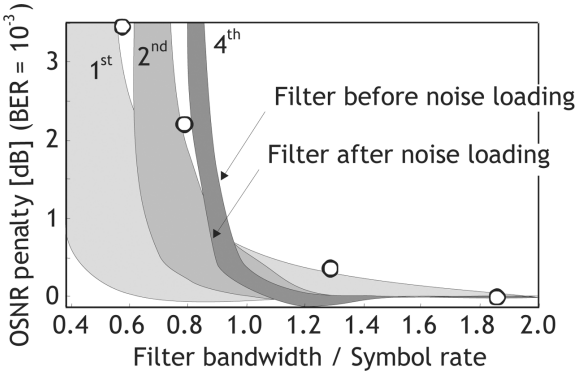

Fig. 8. Tolerance of the system to narrowband optical filtering. Symbols are experimental measurements. Shaded areas are simulations for 1st, 2nd, and 4th order super-Gaussian filters, bounded by the two extreme cases where filtering takes place before noise loading and after noise loading, respectively.

of 1st, 2nd, and 4th order, with the normalized 3-dB filter bandwidth shown on the x-axis. Depending on whether the OSNR degradation takes place before or after the narrowband filter, different results are obtained. (In practice, noise will be added both before and after the several filters present in a system, so that the actual performance of an optically-routed system is expected to fall in between these two extremes). In general, worse results are obtained when introducing noise *after* narrowband filtering, since in this case the strongest noise-enhancement effect due to the adaptive equalizer within the coherent receiver is observed. Noise enhancement is not observed when the OSNR is degraded *before* narrowband filtering, since in this case the filter acts on both signal and noise and the equalizer re-establishes white noise conditions while simultaneously equalizing the signal. The symbols are experimental measurements using two 50 GHz/100 GHz interleavers that were detuned relative to each other, thereby emulating narrow optical filters of 8, 11, 18, and 26 GHz bandwidth, albeit with varying filter shapes. Noise loading was performed after filtering in these experiments, and a reasonable agreement between measurement and simulation is observed.

V. WDM Experiments

For all our WDM experiments we used the experimental setup shown in Fig. 9. Ten lasers were operated on the desired WDM grid in the C band (193.300–193.525 THz for experiments on a 25-GHz grid and 193.35 THz–193.50 THz for a 16.67-GHz grid). Of these, 9 were distributed feedback (DFB) lasers, while a tunable external-cavity laser (ECL) with a 3-dB linewidth of ∼100 kHz was used for the respective channel under test. The sets of even and odd channels were each generated using a separate transmitter of the type shown in Fig. 2. Odd and even channels were amplified using erbium-doped fiber amplifiers (EDFAs) and combined by a symmetric interleaver (IL), 25 GHz/50 GHz for our 25-GHz spaced WDM experiments and 16.7 GHz/33.4 GHz for our 16.67-GHz spaced WDM experiments. In our 1022-km transmission experiment, a simple 3-dB coupler was used for WDM combination, enabled by the electronic waveform shaping through electrical low-pass filtering of the drive signal.

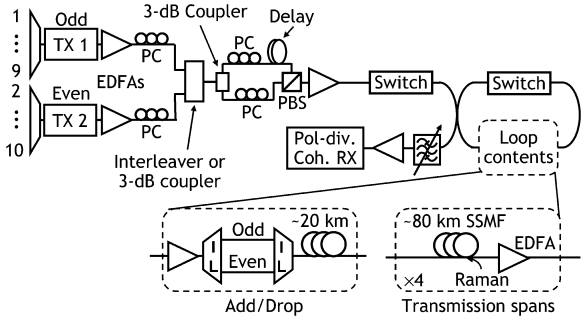

Fig. 9. Experimental setup used for all our WDM experiments.

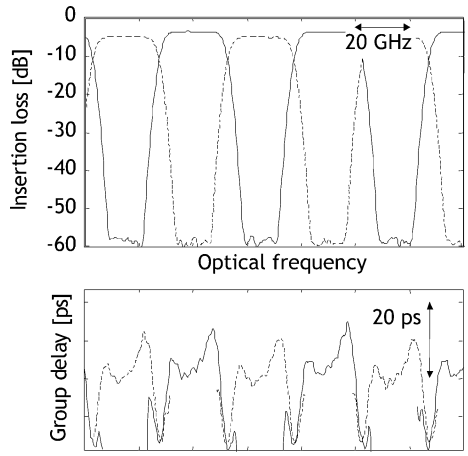

Fig. 10. Magnitude and group delay response of the 25-GHz interleavers used in our experiments.

After WDM-combination, the signals were polarization-multiplexed by splitting into two paths and recombining in a polarization beamsplitter (PBS), using manual polarization controllers (PCs) and a decorrelation delay of ∼20 ns (280 symbols). The recirculating loop contained different optical elements, depending on the respective experiment:

- In the filter-concatenation experiment (Section V.A, [14]), the loop contained a short (20-km) span of standard single-mode fiber (SSMF) together with an add/drop node composed of two 25 GHz/50 GHz interleavers. Fig. 10 gives magnitude and group delay characteristics of an individual such interleaver. The 3-dB bandwidth of the full node is 20.6 GHz.
- In the long-haul transmission experiment (Section V.C [16]) as well as in the ultrahigh spectral efficiency experiment (Section V.D [15]), the loop contained four ∼80-km spans of SSMF (total loop length of 315 km) and a gain-equalizing filter. The loss of the spans ranged from 16 dB to 17 dB. Amplification was provided by backward Raman pumping and EDFA repeaters with approximately 5-dB noise figures. No dispersion-compensating fiber was used. In the long-haul transmission experiment, a coupler was placed after the amplifier following the first span, and was used to sample the signals after transmission over thirteen spans (3 complete loops $+1$ span $= 1022$ km).

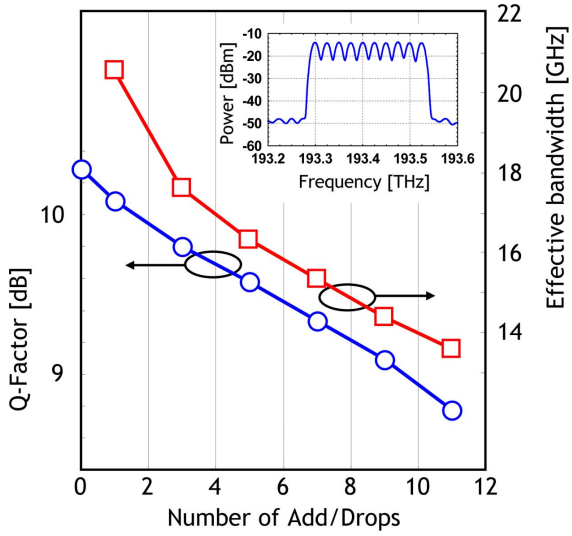

Fig. 11. Results of a filter concatenation experiment in a 10-channel 25-GHz WDM environment (inset). The performance (measured BER expressed in terms of the Q-factor) is shown on the left axis as a function of the number of add/drop nodes passed, and the concatenated filter bandwidth (corrected compared to [14]) is shown on the right axis.

At the receiver, the test channel, including a portion of its neighbors, was selected using a 0.25-nm-bandwidth optical filter, amplified, and combined with a LO in a coherent detection setup according to Fig. 3.

A. Filter Concatenation on a 25-GHz WDM Grid

Figure 11 shows the results of a filter concatenation experiment [14], represented in terms of the received Q-factor. With all 10 channels on (cf. inset), WDM crosstalk results in a BER floor at 5×10^{-4} (Q-factor of 10.38 dB). The observed performance degradation represents a combination of filter concatenation, WDM crosstalk, and reduced OSNR as the number of loop round-trips increases. After 7 passes through the add/drop node, the Q-factor is reduced to 9.38 dB (BER of 1.7×10^{-3}), representing a penalty of 1 dB. Also shown in the figure is the concatenated optical filter bandwidth as a function of the number of nodes passed. For 10 filter passes, the bandwidth shrinks to about 70% of its starting value. Note that the adaptive equalizer in the coherent receiver also compensates well for a significant amount of group delay ripple of the optical filters (cf. Fig. 10), which adds approximately linearly for each loop round-trip. ('Approximately' due to the slight frequency shift imposed by the acousto-optic switches for each loop round trip).

Then, the 10 channels were transmitted through a straight line of four ∼80-km spans of SSMF (a total of 315 km) with EDFA-only repeaters and no dispersion-compensating fiber. An add/drop node was included after the second span. The per-channel power launched into each span was -4 dBm, yielding a BER of 1.8×10^{-3} for the test channel at a received OSNR of 28 dB.

B. Electronic Pulse-Shaping: 25-GHz WDM Without ILs

The BER floor due to WDM crosstalk observed in the previous experiment was eliminated by using electrical low-pass filtering prior to modulation, which shapes the optical spectrum

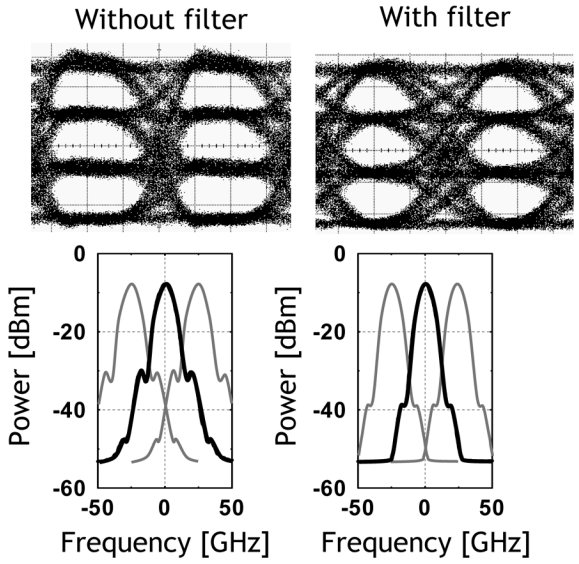

Fig. 12. Effect of electronic pulse shaping on 4-level drive signal eye diagrams and on 16-QAM optical spectra. Pulse shaping significantly reduces WDM crosstalk, as can be seen from the 25-GHz spaced neighbors shown in gray.

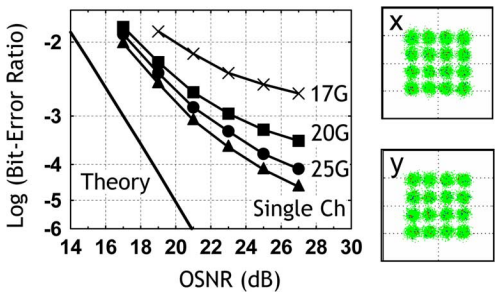

Fig. 13. BER measurements for colorless (interleaver-free) WDM combination and for WDM channel spacings of 25 GHz, 20 GHz, and 17 GHz.

by curtailing its sidelobes. As shown in Fig. 2, simple passive Gaussian electrical low-pass filters with bandwidths of approximately 11 GHz were used to this end, avoiding more sophisticated high-speed digital pulse shaping through digital-to-analog conversion of programmed raised-cosine waveforms [8], [9]. The four-level eye diagrams of the shaped and unshaped modulator drive signals as well as of the corresponding optical spectra are shown in Fig. 12.

The good suppression of spectral side lobes allowed us to combine WDM channels on a 25-GHz WDM grid *without* the use of interleavers, using a simple 3-dB coupler. Fig. 13 shows BER measurements for this case. The triangles represent the reference single-channel measurement of PDM 16-QAM, revealing a back-to-back required OSNR of 20.8 dB to achieve a BER of 1×10^{-3}, which is about 1.2 dB better than our first results shown in Fig. 6, and is off the theoretical limit (solid line) by 3.8 dB. In 25-GHz WDM operation (circles), WDM crosstalk from the two nearest neighbors imposes an additional penalty of 1 dB. The penalty rises rapidly for WDM channel spacings below 20 GHz (see curves in Fig. 13 for 20-GHz and 17-GHz spacing). The recovered 16-QAM signal constellations of a central WDM channel at 25-GHz spacing and 21-dB OSNR (BER of 1.3×10^{-3}) are also shown.

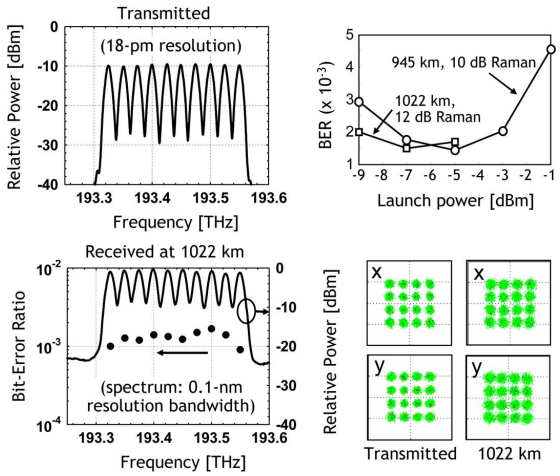

Fig. 14. Transmitted and received WDM spectra on a 25-GHz grid after 1022-km transmission. Upper right: Optimization of Raman gain and per-channel signal launch power. BER results after transmission are shown in the lower left plot together with the received spectrum. Lower right: Recovered symbol constellations before and after transmission.

C. Long-Haul Transmission on a 25-GHz WDM Grid

We performed transmission of 10 WDM channels on a 25-GHz grid over 945 km (3 full loops) as well as over 1022 km (3 full loops plus one span). Fig. 14 summarizes the results of the WDM experiment. The figure shows the transmitted and received WDM spectra after 1022 km (using optical spectrum analyzers with different resolutions). The upper right portion of the figure shows the received BER as a function of the per-channel signal launch power. At 945 km, the optimum launch power is -5 dBm at a Raman gain of 10 dB. For 1022-km transmission we increased the Raman gain to 12 dB and found an optimum launch power of -7 dBm. After 1022-km transmission, the average OSNR of the channels was 24 dB. The BER of each of the ten channels is shown together with the received spectrum in the lower left portion of Fig. 14. The highest BER is 1.8×10^{-3}, below the correction threshold of 2×10^{-3} of enhanced FEC with 7% overhead. The recovered signal constellations for channel 5 are shown at the transmitter and after 1022-km transmission.

D. WDM Transmission at 6.2 b/s/Hz Spectral Efficiency

As evident from Fig. 13, going below 25-GHz channel spacing requires additional optical interleaver filtering at the transmitter to avoid significant WDM crosstalk penalties. In order to achieve 16.67-GHz channel spacing with low penalties, we therefore used a custom-designed silica-on-silicon, 0.80% normalized-index-step planar-lightwave circuit with highly sampled arrayed-waveguide gratings (AWGs) in a configuration similar to [34] and [35]. It consists of two AWGs with a free-spectral range of 33.33 GHz and 14 grating arms each connected by 7 equal-length waveguides. The magnitude and group-delay responses of the interleaver passbands, with a 3-dB bandwidth of 13 GHz are shown in Fig. 15.

Fig. 16 shows back-to-back BER measurements. The triangles represent the measurement of a single-channel PDM 16-QAM signal without using the 16.67-GHz/33.33-GHz

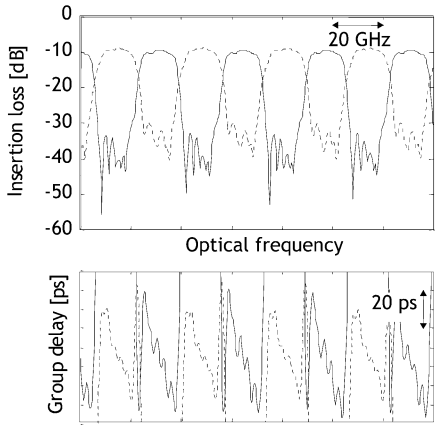

Fig. 15. Magnitude and group delay response of the 16.67-GHz interleaver used in our experiments.

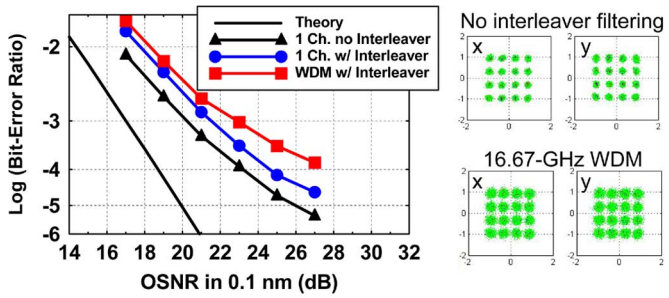

Fig. 16. BER measurements of 16-QAM for 16.67-GHz spaced WDM. Solid curve: Theory; Triangles: Single channel, no interleaver; Circles: Single channel, 16.67-GHz interleaver; Squares: WDM on a 16.67-GHz grid.

interleaver, revealing a back-to-back required OSNR ($\mathrm{BER} = 10^{-3}$) of 20.2 dB, another 0.6-dB improvement compared to the results of Section V.B and only 3.2 dB off the theoretical limit, solid line. When passing through the interleaver (circles), a penalty of 1.3 dB is incurred due to the tight optical filtering, in line with the results of Fig. 8. Crosstalk from the 33.3-GHz spaced neighbors within the same set of WDM channels (i.e., for operation with even channels only or with odd channels only) was measured to be negligible. In 16.7-GHz WDM operation (squares), crosstalk from the two nearest neighbors imposes an additional penalty of 1.5 dB. Fig. 16 also shows the recovered 16-QAM signal constellations for both polarizations of a single unfiltered channel at high (~35 dB) OSNR as well as for a central WDM channel at 23-dB OSNR (BER of 1×10^{-3}).

After 630-km transmission (2 loop round-trips; 10-dB Raman gain; −7 dBm per-channel signal launch power), the average OSNR of the channels was 24 dB. Transmitted and received spectra are shown in Fig. 17 (using optical spectrum analyzers with different resolutions). The received signal constellations of a central channel are also shown, together with the BER of each of the 10 channels. All BERs are below 2×10^{-3}, the threshold of enhanced FEC.

VI. Conclusion

We have summarized a series of experiments [14]–[16] that demonstrated the first blind intradyne detection of PDM

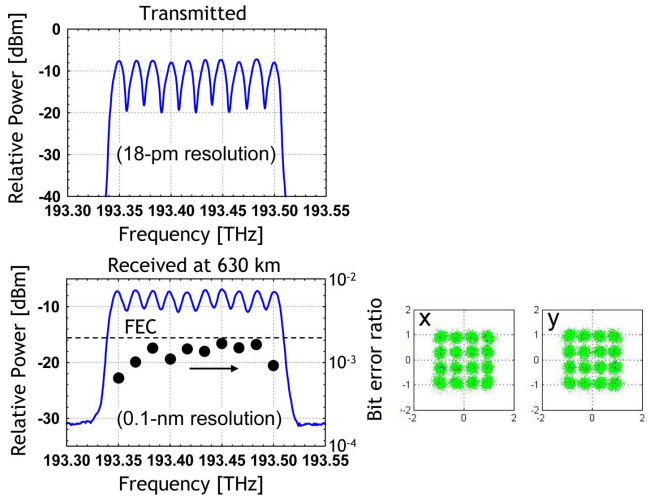

Fig. 17. Transmitted and received WDM spectra on a 16.67-GHz grid after 630-km transmission. BER results after transmission are shown in the lower left plot together with the received spectrum. Lower right: Recovered symbol constellations after transmission.

16-QAM signals at 112 Gb/s. We have described transmitter and receiver setups as well as the underlying detection algorithms in detail and analyzed their performance using both simulated and measured waveforms. Our receiver requires an ADC resolution of 5 bits and a frequency difference between signal and LO lasers of below ~20 MHz. The aggregate linewidth of the two lasers must stay below several hundred kHz in order to avoid noticeable OSNR penalties. The entire setup yields a back-to-back required OSNR of 20.2 dB, which is 3.2 dB off the theoretical limit.

In a 25-GHz-spaced 10-channel WDM environment (4.1 b/s/Hz), we measured a 1-dB Q-factor penalty after seven passes through an add/drop multiplexer, and transmitted the signal over 1022 km of uncompensated, hybrid EDFA-Raman amplified 80-km spans of SSMF. Electrical waveform shaping allowed us to combine the WDM channels using a simple 3-dB coupler and no optical interleaver filters.

On a 16.67-GHz WDM grid, we achieved 10-channel transmission over 630 km using the same line system as for the 1022-km experiment. This yields a high spectral efficiency of 6.2 b/s/Hz, with 1-Tb/s of information fitting within 1.2 nm of optical bandwidth. A spectral efficiency × distance product of 3906 b/s/Hz × km was obtained.

Acknowledgment

The authors thank R. W. Tkach for valuable discussions; V. Faraci and G. Rodet for providing 25-GHz interleavers; and M. Cappuzzo, E. Y. Chen, L. T. Gomez, F. Klemens, and R. Keller for 16.67-GHz silica waveguide interleaver fabrication.

References

[1] R. W. Tkach, "Scaling optical communications for the next decade and beyond," *Bell Labs. Tech. J.*, 2010, to appear in.
[2] P. J. Winzer and R.-J. Essiambre, "Advanced optical modulation formats," *Proc. IEEE*, vol. 94, pp. 952–985, 2006.
[3] R. A. Griffin and A. C. Carter, "Optical differential quadrature phase shift keying (oDQPSK) for high-capacity optical transmission," in *Proc. OFC*, 2002, pp. 367–368, WX6.

[4] A. H. Gnauck, G Charlet, P. Tran, P. J. Winzer, C. R. Doerr, J. C. Centanni, E. C. Burrows, T. Kawanishi, T. Sakamoto, and K. Higuma, "25.6-Tb/s WDM transmission of polarization-multiplexed RZ-DQPSK signals," *J. Lightw. Technol.*, vol. 26, pp. 79–84, 2008.

[5] A. H. Gnauck, P.J. Winzer, C. Dorrer, and S. Chandrasekhar, "Linear and nonlinear performance of 42.7-Gb/s single-polarization RZ-DQPSK format," *Photonics Technology Letters*, vol. 18, no. 7, pp. 883–885, Apr. 1, 2006.

[6] C. R. S. Fludger, T. Duthel, D. van den Borne, C. Schulien, E.-D. Schmidt, T. Wuth, J Geyer, E. De Man, G.-D. Khoe, and H. de Waardt, "Coherent equalization and POLMUX-RZ-DQPSK for robust 100-GE transmission," *J. Lightw. Technol.*, vol. 26, no. 1, pp. 64–72, Jan. 2008.

[7] P. J. Winzer, "Modulation and multiplexing in optical communication systems," LEOS Newsletter Feb. 2009 [Online]. Available: http://www.ieee.org/organizations/pubs/newsletters/leos/feb09/index.html, on-line at

[8] R.-J. Essiambre, G. J. Foschini, G. Kramer, and P. J. Winzer, "Capacity limits of fiber-optic networks," *Phys. Rev. Lett.*, vol. 101, p. 163901, 2008.

[9] R.-J. Essiambre, G. Kramer, P. J. Winzer, G. J. Foschini, and B. Goebel, "Foundations for determining capacity limits of fibers," *J. Lightw. Technol.*, 2009, accepted for publication.

[10] M. Nakazawa, "Optical quadrature amplitude modulation (QAM) with coherent detection up to 128 states," in *Proc. OFC'09*, 2009, OThG1.

[11] H. Takahashi, A. Al Amin, S. Jansen, I. Morita, and H. Tanaka, "Highly Spectrally Efficient DWDM Transmission at 7.0 bit/s/Hz using 8 x 65.1-Gbit/s Coherent PDM-OFDM," *J. Lightw. Technol.*, vol. 28, no. 4, Feb. 2010.

[12] X. Zhou, J. Yu, D. Qian, T. Wang, G. Zhang, and P. Magill, "8 × 114 Gb/s, 25-GHz-spaced, PolMux-RZ-8PSK transmission over 640 km of SSMF employing digital coherent detection and EDFA-only amplification," in *Proc. OFC*, 2008, PDP1.

[13] X. Zhou, J. Yu, M.-F. Huang, Y. Shao, T. Wang, P. Magill, M. Cvijetic, L. Nelson, M. Birk, G. Zhang, S. Ten, H. Matthew, and S. Mishra, "Transmission of 32-Tb/s Capacity Over 580km Using RZ-Shaped PDM-8QAM Modulation Format and Cascaded Multi-Modulus Blind Equalization Algorithm," *J. Lightw. Technol.*, vol. 28, no. 4, Feb. 2010.

[14] P. J. Winzer and A. H. Gnauck, "112-Gb/s polarization-multiplexed 16-QAM on a 25-GHz WDM grid," in *Proc. ECOC*, 2008, Th.3.E.5.

[15] A. H. Gnauck, P. J. Winzer, C. R. Doerr, and L. L. Buhl, "10 × 112-Gb/s PDM 16-QAM transmission over 630 km of fiber with 6.2-b/s/Hz spectral efficiency," in *Proc. OFC'09*, 2009, PDPB8.

[16] A. H. Gnauck and P. J. Winzer, "10 × 112-Gb/s PDM 16-QAM transmission over 1022 km of SSMF with a spectral efficiency of 4.1 b/s/Hz and without optical filtering," in *Proc. ECOC'09*, 2009, paper 8.4.2.

[17] J. R. Treichler, M. G. Larimore, and J. C. Harp, "Practical blind demodulators for high-order QAM signals," *Proc. IEEE*, vol. 86, no. 10, pp. 1907–1926, 1998.

[18] C. R. Johnson, P. Schniter, T. J. Endres, J. D. Behm, D. R. Brown, and R. A. Casas, "Blind equalization using the constant modulus criterion: A review," *Proc. IEEE*, vol. 86, no. 10, pp. 1927–1950, 1998.

[19] N. K. Jablon, "Joint blind equalization, carrier recovery, and timing recovery for high-order QAM signal constellations," *IEEE Trans. Signal Process.*, vol. 40, no. 6, pp. 1383–1398, Jun. 1992.

[20] S. J. Savory, "Digital filters for coherent optical receivers," *Opt. Exp.*, vol. 16, no. 2, pp. 804–817, 2008.

[21] J. Yang, J.-J. Werner, and G.A. Dumont, "The multimodulus blind equalization and its generalized algorithms," *IEEE J. Selec. Areas in Communications*, vol. 20, no. 5, pp. 997–1015, Jun. 2002.

[22] X. Zhou, J. Yu, and P. D. Magill, "Cascaded two-modulus algorithm for blind polarization de-multiplexing of 114-Gb/s PDM-8-QAM optical signals," in *Proc. OFC'09*, 2009, Paper OWG3.

[23] W. A. Sethares, G. A. Rey, and C. R. Johnson, Jr., "Approaches to blind equalization of signals with multiple modulus," in *Proc. ICASSP'89*, 1989, Paper D3.21.

[24] M. J. Ready and R. P. Gooch, "Blind equalization on radius directed adaptation," in *Proc. ICASSP'90*, 1990, Paper D11.16.

[25] H. Louchet, K. Kuzmin, and A. Richter, "Improved DSP algorithms for coherent 16-QAM transmission," in *Proc. ECOC'08*, 2008, Paper Tu.1.E.6.

[26] M. Seimetz, "Performance of coherent optical square-16-QAM-systems based on IQ-transmitters and homodyne receivers with digital phase estimation," in *Proc. OFC'06*, 2006, Paper NWA4.

[27] R. A. Axford, L. B. Milstein, and J. R. Zeidler, "A dual-mode algorithm for blind equalization of QAM signals: CADAMA," in *Proc. Conf. Rec. 29th Asilomar Conf. Signals, Syst. Comput.*, 1995, p. 172.

[28] A. Spalvieri and R. Valtolina, "Data-Aided and Phase-Independent Adaptive Equalization for Data Transmission Systems," European Patent Application EP 1 089 457 A2, 2000.

[29] T. Pfau, S. Hoffmann, and R. Noe, "Hardware efficient coherent digital receiver concept with feedforward carrier recovery for M-QAM constellation," *J. Lightw. Technol.*, vol. 27, no. 8, pp. 989–999, Apr. 2009.

[30] E. Ip and J. M. Kahn, "Feedforward carrier recovery for coherent optical communication systems," *J. Lightw. Technol.*, vol. 25, no. 9, pp. 2675–2692, Sep. 2007.

[31] J. G. Proakis, *Digital Communications*. New York: McGraw Hill, 2001.

[32] M. Seimetz, "Laser linewidth limitations for optical systems with high-order modulation employing feed forward digital carrier phase estimation," in *Proc. OFC'08*, 2008, Paper OTuM2.

[33] Y. Mori *et al.*, "Phase-noise tolerance of optical 16-QAM signals demodulated with decision-directed carrier-phase estimation," in *Proc. OFC'09*, 2009, Paper OWG7.

[34] C. R. Doerr, R. Pafchek, and L. W. Stulz, "Integrated band demultiplexer using waveguide grating routers," *IEEE Photon. Technol. Lett.*, vol. 15, no. 8, pp. 1088–1090, Aug. 2003.

[35] C. R. Doerr, L. L. Buhl, M. A. Cappuzzo, E. Y. Chen, L. T. Gomez, F. P. Klemens, and R. C. Keller, "Interleaver Using an Arrayed-Waveguide Grating-Lens-Grating Configuration for Spectrally Efficient Systems," *IEEE Photon. Technol. Lett.*, vol. 22, no. 1, pp. 6–8, Jan. 2009.

Peter J. Winzer (S'93-A'99-SM'05-F'09) received the Ph.D. degree in electrical/communications engineering from the Vienna University of Technology, Vienna, Austria, in 1998. His academic work, largely supported by the European Space Agency (ESA), was related to the analysis and modeling of space-borne Doppler wind lidar and highly sensitive free-space optical communication systems.

In this context, he specialized on advanced digital optical modulation formats and high-sensitivity optical receivers using coherent and direct detection. After joining Bell Labs in November 2000, he focused on various aspects of high-bandwidth optical communication networks, including Raman amplification, optical modulation formats, advanced optical receiver concepts, and digital signal processing at bit rates from 10 to 100-Gb/s. He has widely published in peer-reviewed journals and at conferences and holds several patents in the fields of optical communications, lidar, and data networking.

Dr. Winzer is actively involved as a Reviewer, Associate Editor, and Committee Member of various journals and conferences and serves as an elected member of the IEEE-LEOS BoG. He is a Distinguished Member of technical Staff at Bell Labs, a Member of the Optical Society of America (OSA).

Alan Gnauck (M'98-SM'00-F-09) joined Bell Laboratories in 1982, where he is currently a Distinguished Member of Technical Staff in the Transmission Systems and Networks Research group.

He has performed record-breaking optical transmission experiments at single-channel rates of from 2 to 160 Gb/s. He has investigated coherent detection, chromatic-dispersion compensation techniques, CATV hybrid fiber-coax architectures, wavelength-division-multiplexing (WDM) systems, and system impacts of fiber nonlinearities. His WDM transmission experiments include the first demonstration of terabit transmission. More recently, he has demonstrated 25-Tb/s transmission. He is presently involved in the study of WDM systems with single-channel rates of 40 Gb/s and higher, using various modulation formats. He has authored or co-authored over 180 journal and conference papers, and holds 23 patents in optical communications.

Mr. Gnauck is a Fellow of the Optical Society of America (OSA), a Fellow of the Institute of Electrical and Electronic Engineers (IEEE), and former Associate Editor for IEEE Photonics Technology Letters (2000–2009).

Christopher R. Doerr (F'06) received the B.S. degree nautical/astronautical engineering and the B.S., M.S., and Ph.D. degrees (1995) in electrical engineering, all from the Massachusetts Institute of Technology (MIT), Cambridge. He attended MIT on an Air Force ROTC scholarship and earned his pilot wings at Williams AFB, Arizona, in 1991. His Ph.D. thesis, on constructing a fiber-optic gyroscope with noise below the quantum limit, was supervised by Prof. H. Haus.

Since joining Bell Labs in 1995, Doerr's research has focused on integrated devices for optical communication. He was promoted to Distinguished Member of Technical Staff in 2000,

Dr. Doerr received the OSA Engineering Excellence Award in 2002, became an IEEE Fellow in 2006 and an OSA Fellow in 2009, and received in the IEEE William Streifer Award in 2009. He was Editor-in-Chief of IEEE Photonics Technology Letters from 2006–2008 and is currently an Associate Editor for the IEEE/OSA JOURNAL OF LIGHTWAVE TECHNOLOGY.

Maurizio Magarini was born in Milano, Italy, in 1969. He received the M.S. and Ph.D. degrees in electronic engineering from the Politecnico di Milano, Milano, Italy, in 1994 and 1999, respectively.

In 1994, he was granted the TELECOM Italia scholarship award for his Master thesis. From 1999 to 2001 he was a Research Associate in the Dipartimento di Elettronica e Informazione at the Politecnico di Milano where, since 2001, he has been an Assistant Professor. From August 2008 to January 2009 he spent a sabbatical leave at Bell Labs, Alcatel-Lucent, Holmdel, NJ. He has authored and coauthored more than 30 journal and conference papers. His research interests are in the broad area of communication theory. Topics include synchronization, channel estimation, equalization, coding and reduced complexity detection schemes for multi-antenna systems.

Lawrence L. Buhl (Larry) received a B.Sc. in electronic engineering from Monmouth University, Long Branch, NJ, in 1984.

He first served in the US Army, Signal Corp, Fort Monmouth, NJ, as an instructor, teaching Microwave theory and Radar systems. He joined Bell Laboratories in 1972, beginning early research work in metal vapor laser spectroscopy. In 1978, he began pioneering and developed various guided wave optical devices in $LiNbO_3$ and later, III-V materials. Since 2000, he has been investigating 10G and 40G systems and devices and recently assumed responsibility for optical and high speed device packaging.